Article

Not peer-reviewed version

The Role of the Manganese Content on the Properties of Mn3O4 and Reduced Graphene Oxide Nanocomposites for Supercapacitor Electrodes

Víctor Fernández-Jiménez , Santiago De Bernardi-Martín , Alejandra García-Gómez , David López-Diaz , M. Jesús Sánchez-Montero , M. Mercedes Velázquez , M. Dolores Merchán *

Posted Date: 19 July 2024

doi: 10.20944/preprints202407.1586.v1

Keywords: supercapacitors; electrodes; graphene oxide; transition metal oxides; hybrids; charge store mechanisms doi:10.20944/preprints202407.1586.v1

Article

The Role of the Manganese Content on the Properties of Mn_3O_4 and Reduced Graphene Oxide Nanocomposites for Supercapacitor Electrodes

Víctor Fernández-Jiménez [1], Santiago de Bernardi-Martín [2], Alejandra García-Gómez [2], David López-Díaz [1,3,4], M. Jesús Sánchez-Montero [1,3,4], M. Mercedes Velázquez [1,3,4] and M. Dolores Merchán [1,3,4,*]

[1] Departamento de Química Física, Facultad de Ciencias Químicas, Universidad de Salamanca, E37008, Salamanca, Spain
[2] Gnanomat S.L., Madrid, E28049 Spain
[3] Grupo de Nanotecnología, Universidad de Salamanca, E37008, Salamanca, Spain
[4] Laboratorio de Nanoelectrónica y Nanomateriales, USAL-NANOLAB, Universidad de Salamanca, E37008, Salamanca, Spain
* Correspondence: mdm@usal.es; ORCID: 0000-0003-3573-3805

Abstract: Increasing the energy density and power of supercapacitors through hybrids of carbonaceous materials and metal oxides continues to be the subject of numerous research works. The correlation between specific capacitance and the properties of materials used as electrodes attracts great in-terest. In the present study, we have investigated composites (GO/Mn3O4) prepared by hydro-thermal method with variable ratio GO/Mn3O4 and tested as supercapacitor electrode materials in three and two-electrode cells. The chemical characterization carried out by X-ray Photoelectron Spectroscopy and the adsorption techniques used have allowed the determination of the surface carbon and oxygen content, as well as its textural properties. In this work we have analyzed the contribution of the double layer and of the Faradaic reactions to the value of the final capacitance of the synthesized materials. Beyond empirically obtaining the electrochemical properties, these have been related to the physicochemical characteristics of the hybrids, to help design materials with the best performances for supercapacitor electrodes

Keywords: supercapacitors; electrodes; graphene oxide; transition metal oxides; hybrids; charge store mechanisms

---

1. Introduction

The high demand for energy to meet the needs of humanity, and the evidence of the damage that the combustion of fossil fuels causes to the environment [1], has tipped the balance towards clean forms of energy such as solar and wind power. The intermittency of this type of energy dictates the need to develop electrical energy stor-age devices, such as lithium-ion batteries (LiB) and supercapacitors [2,3]. The scien-tific community has proposed supercapacitors as an individual solution or combined with other storage devices [3–5]. Supercapacitors have several advantages including high power density, quick charge-discharge time, superior specific capacitance, low input resistance, long lifetime and are environment-friendly [3,4,6]. Supercapacitors are the bridge between capacitors with high power density and batteries/fuel cells with high energy density [7–9]. Supercapacitors have greater energy density than capaci-tors, but lower power density. Compared with conventional batteries, supercapacitors present a charge-discharge cycle life almost unlimited [10] have higher power density but lower energy density [9].

The capacitance of a supercapacitor arises from two different basic mechanisms, the electrochemical double layer capacitance (EDLC) due to the separation of electrical charges at the Helmholtz layer, and from the pseudo capacitance involving electro-chemical Faradaic reactions (FR) in which a chemical reaction takes place in the elec-trode, and the storage of electrical charge is carried out electrostatically, without in-teraction between electrode and ions.

The search for new materials for supercapacitor electrodes is based on the modi-fication of the precursors and on obtaining materials with high power, high energy density, fast charging and discharging and good tolerance to cycles [11]. Carbonaceous materials such as biomass activated carbons [12–14], graphene [15–19], carbon cloths [20], carbon nanotubes [21–23], have high conductivity, low cost and high specific sur-face area. In these materials the predominant mechanism is EDLC; however, they have low capacitance [23]. Current research attempts to modify the structure and texture of these materials to, in turn, increase the specific capacitance. There are also many attempts to combine them with transition metal oxides, which increases their operating voltage range and the specific capacitance [11,24]. Transition metal oxides present apparent advantages, including a variety of oxidation states [25–27], high specific ca-pacitance and conductivity and low resistance, what make them very good candidates as electrodes for supercapacitors [28]. Manganese oxide, cobalt oxide, nickel oxide, zinc oxide, ruthenium oxide, among others, have been widely studied [24,29–34]. However, although the energy density provided by pseudocapacitive materials is always greater than the capacitance due to the double layer of EDLC provided by carbonaceous mate-rials, they have lower stability due to the action Faradaic reactions [19,22,35,36]. Hy-brid supercapacitors aim to combine the advantages of both mechanisms by integrat-ing carbon-based materials with metal oxide materials, thus incorporating physical and chemical charge storage mechanisms together in a single electrode [10,35,36]. Carbon-based materials provide a high surface area that increases the contact between the deposited pseudocapacitive materials and the electrolyte, and pseudocapacitive materials enhance the electrode capacitance through Faradaic reactions [37–39].

Manganese is an abundant, environmentally friendly, low-cost element with high theoretical specific capacitance, however, its performance is limited when a high-power supercapacitor is required, since it presents low electronic and ionic con-ductivity [11]. In an attempt to achieve more electroactive sites and faster ion transport, there are several works about Mn3O4 [40–42] with a porous structure, achieving a significant improvement in electrochemical performance. Hausmannite or manganese oxide (Mn3O4) is a widely studied electrode material because of its fasci-nating features such as high theoretical capacitance and variable oxidization states [43]. The improvement is even more significant when hybrids are prepared with gra-phene and graphene derivatives [42,44–48]. In the works found on hybrids based on reduced graphene oxide, rGO and transition metal oxides, TMO, it has been shown that the specific surface area and pore size distribution of the material play key roles in the capacitive behavior [11,44,49]. The distribution of TMO on a large surface substrate provides better electrical contact and improves the diffusion of the electrolyte to the active material. It has also been reported that the properties of the hybrids depend on the conditions of formed graphene, defects, composition, etc. [44].

Many researchers have developed hybrids of Mn3O4 with great potential as energy storage with graphene derivatives, with excellent conductivity. Wang et al. [50] re-ported for the first time the preparation of graphene on the surface of Mn3O4 by CVD obtaining a specific capacitance of 208.3 F g-1 at 0.5 A g-1, and Jia et al. [51] prepared Mn3O4/rGO hybrids using a template method, reaching the material 561 F g-1 at a cur-rent density of 1A g-1. However, due to the complex methods of synthesis, and the dif-ficulty to control the structure of the material, it remains a challenge to develop a sim-ple method to prepare Mn3O4/rGO with control on the electrochemical properties.

Finding a good material involves understanding the delicate balance between the two mechanisms that can participate in the charge accumulation process, EDLC and Faradaic reactions, and designing the best possible material requires knowing the role that each component plays in each of these mechanisms. As far as we know, there are no systematic studies of this type in the literature. With this objective in mind, in this work we have prepared hybrids with different proportions of Mn3O4 nanoparticles decorating the surface of reduced graphene oxide by a simple hydrothermal method. The hybrids were characterized by Raman and XPS spectroscopies, XRD and gas ad-sorption of N2 and CO2. The variable amounts of Mn3O4 lead to hybrids with different electrochemical behavior tested by cyclic voltammetry and galvanostatic charge-discharge measurements. This study has allowed us to know the role that the two components of the hybrids play in the charge storage mechanisms, and the con-tribution of each of them to the specific capacitance. This will help to design reduced graphene oxide/Mn3O4 hybrid materials with the best electrochemical performance for supercapacitor electrodes.

2. Materials and Methods

2.1. Materials and Reagents

Graphene oxide was synthesized by the oxidation of natural graphite flakes (CAS 7782-42-5) from Sigma Aldrich. The reagents used for graphite oxidation and for the preparation of hybrids were NaNO3 (99 %), H2SO4 (98 %w), KMnO4 (> 99 %), H2O2 (30 %V), Manganese acetate Mn(CH3COO)2.4H2O (> 99 %), were purchased from Sigma Aldrich (St. Louis, MO). NaOH (>97%), was supplied by Panreac Química SLU (Barcelona, Spain). For electrochemical characterization the reagents used were Poly (vinylidene fluoride) PVDF from Sigma Aldrich, tetraethylammonium tetrafluorobo-rate Et4NBF4 from Alfa Aesar, and acetonitrile (CAN) HiPerSolv CHROMANORM® purchased from VWR). All reagents were used without purification.

We used Ultra-pure water from a RiOs and Milli-Q combined system from Milli-pore. Carbon dioxide (CO2), nitrogen (N2), and helium (He) were supplied by L'Air Liquide, Madrid, Spain. The minimum purity was 99.999%.

2.2. Synthesis of Graphene Oxide, Metal Oxides and Graphene Oxide/Metal Oxide Hybrids

Graphene oxide (GO) was obtained through the oxidation procedure reported by Hummers modified by our group [52–55]. The preparation of the Graphene Ox-ide/Manganese Oxide Hybrids was carried out from acetate of manganese. An aqueous solution of NaOH (0.1M) was added dropwise to a solution of Mn(CH3COO)2.4H2O (5mg/ml) until the pH value was approximately 12. On the colloidal solution obtained, added a certain volume of the aqueous dispersion of GO (1mg/mL). The mixture was diluted to 30 mL with ultrapure water and stirred for 6 hours. Subsequently, the mix-ture was transferred to a 110 mL stainless steel Teflon-lined autoclave and heated to 180°C at 2°C/min for 12 hours [56]. The graphene oxide/ Mn(CH3COO)2.4H2O weight ratio was modified with the volume of the starting manganese acetate solution, Mn(CH3COO)2.4H2O (5mg/mL), obtaining samples with weight ratio (GO/ Mn(CH3COO)2.4H2O) of (20/ 80), (50/50) and (80/20). Said samples were named GOMn14, GOMn11 and GOMn41 respectively. Since the hydrothermal process drives to reduced graphene oxide [57], for comparative purposes graphene oxide was sub-jected to the same hydrothermal process used for manufacturing the hybrid materials, the reduced GO obtained was called GOH.

2.3. Structural, Chemical and Textural Characterization

X-ray photoelectron spectra (XPS) of powder samples were recorded in a PHI Versa Probe II (Physical Electronics, USA), equipped with an excitation source of Al K (1486.6 eV) at 25 W and a 1.3V and 20.0 µA neutralizer. The high-resolution spec-tra were recorded working at 29.35 eV analyzer pass energy.

Raman spectra were recorded at room temperature with a micro-Raman spec-trometer LabRAM HR Evolution (Horiba Jobin-Yvon). To obtain the Raman spectra of each material, solids are placed onto silicon wafers. Materials were irradiated with 532 nm light from a solid-state laser and a 100x objective (laser spot size 1 µm2). The laser excitation power was kept below 1 mW to avoid laser-induced heating. Calibration was performed by checking the Rayleigh band and Si band at 0 and 520.7 cm-1, respec-tively. The area was scanned with a spatial resolution of approximately 0.5 µm and the acquisition time was 3 s at each point. Each Raman spectrum was recorded at least in five different regions of the samples and spectra shown in figures are the average of all measurements. The diffraction grating used was 1800 gr mm-1 and the spectral resolu-tion with this configuration was 2 cm-1.

Powder XRD patterns were recorded in a Bruker D8 Advance powder diffractom-eter using CuKα1,2 radiation (λ = 1.54050Å) between 5° and 80° (2θ) with a step size of 0.05° and a step time of 2.6 s. The tube operated at 40 kV and 30 mA.

The porous texture of the samples was analyzed from physical adsorption isotherms of N_2 at 77 K and of CO_2 at 273 K, measured in an automatic Micromeritics ASAP 2010 volumetric adsorption apparatus. These isotherms were used to calculate the Specific surface area SBET(N_2), calculated by applying the BET equation to the N_2 adsorption isotherm. Micropore volume was determined from the Dubbinin-Raduskhevic equa-tion to the adsorption isotherms of CO_2, VMP(CO_2) at relative pressures under 0.01 [58,59]. The adsorption of the two gases provides complementary information. Whereas N_2 is adsorbed into micropores larger than 0.7 nm, the adsorption of CO_2 at higher temperature takes place in smaller micropores (<0.7 nm).

2.4. Electrochemical Characterization

The electrochemical performance of the hybrid materials was studied in a three-electrode cell using the Arbin instruments BT-G multichannel potentiostat. For the preparation of the electrodes, synthesized hybrid materials (80 wt. %) were mixed with carbon black (10 wt. %) as conductive material and PVDF binder (10 wt. %). After grinding in an agate mortar, ethanol was added to form a paste. Single-sided coated electrodes were made by depositing the paste on Ni foam with a 1 cm2 area. The elec-trodes were dried at 90ºC overnight. Ag/AgCl electrode and Pt wire were used as reference and counter electrodes, respectively. The electrolyte employed was 1M KOH aqueous solution. Samples were also tested in a two-electrode cell with symmetric con-figuration, using Et_4NBF_4/CAN as non-aqueous electrolyte.

3. Results

3.1. Structural, Chemical, and Textural Characterization of Hybrid Materialssubsection

3.1.1. XPS, Raman Spectroscopy and Gases Adsorption

X-ray photoelectron spectroscopy (XPS) was used to evaluate the surface composition of the nanocomposites. Figure 1a shows the survey spectra of the different materials.

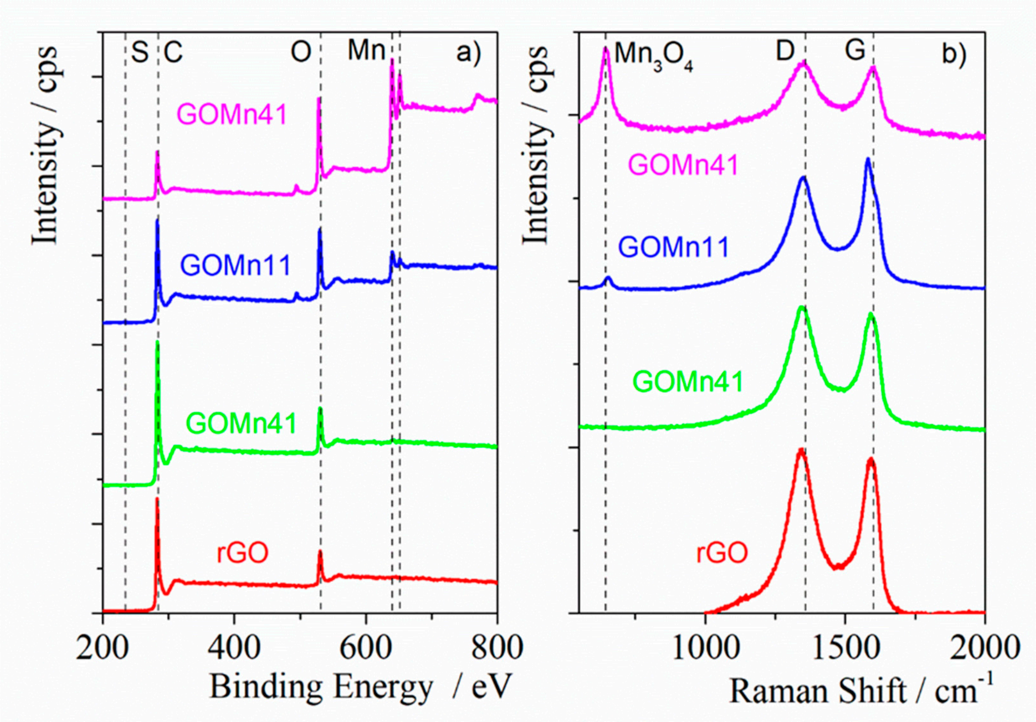

Figure 1. a) XPS survey spectra and b) Raman spectra of rGO/Mn_3O_4 hybrids.

The presence of C, O and Mn atoms was revealed by the survey spectra plotted in Figure 1a. Thus, bands at 285 eV, 530 eV, assigned to C1s and O1s appear in all materials while the two peaks centered at 642 and 653 eV consistent with binding energies of Mn $2p^{3/2}$ and Mn $2p^{1/2}$, respectively, appeared in hybrids and its intensity increases as the percentage of Mn used in the synthesis. The presence of these two bands in the survey spectrum indicates that the main oxidation state of Mn is +4 [60]. The atomic percentage for each element, and the O/C ratio were presented in Table 1. Furthermore, the atomic percentage of Mn obtained by XPS increases as the Mn content used in the synthesis of the hybrid increases.

Specific surface area calculated from the N_2 adsorption and BET model, S_{BET}, and the micropore volume, VMP, obtained from CO_2 adsorption isotherms and the Dubinin–Radushkevich model, are also in Table 1.

Table 1. Atomic composition determined by XPS. Textural characterization by N_2 and CO_2 adsorption.

Materials	**C_{1s} Atomic (%)**	**O_{1s} Atomic (%)**	**Mn_{2p} Atomic (%)**	**O/C**	**S_{BET} (m^2/g)**	**V_{MP} (cm^3/g)**
rGO	88.4 ± 3	11.5 ± 0.9	---	0.13	184	0.06
GOMn41	86.2 ± 4	13.2 ± 0.6	0.50 ± 0.03	0.15	346	0.10
GOMn11	68.8 ± 3	23.1 ± 1	8.0 ± 0.4	0.33	214	0.06
GOMn14	46.4 ± 2	35.5 ± 2	18.0 ± 0.9	0.77	125	0.04

To check if the graphene network was retained after the hydrothermal treatment, Micro-Raman spectra of rGO and the hybrid materials were recorded and plotted in Figure 1b. As can be seen in Figure 1b, the Raman spectra of all materials present the two well defined D, centered around 1350 cm^{-1}, and G, centered close to 1585 cm^{-1} bands characteristic of disordered graphitic materials such as graphene oxide and reduced graphene oxide [53,54,61]. The G band is an allowed band by the selection rules and is assigned to the vibration of the sp^2 carbon lattice. The D band is activated by the presence of defects (holes or functional groups) in the flakes of graphene networks.

The presence of that bands in the Raman spectra means that the disorder graphene network is in the hybrids prepared by the hydrothermal method. In addition, a third band centered at 668 cm^{-1} appears in the spectra of the hybrid materials. This band has been previously reported [62] and was assigned to the stretching vibrations of the metal-oxygen of Mn_3O_4. This demonstrates the formation of Mn_3O_4 in the hybrid materials. As expected, the intensity of this band increases with the proportion of Mn in the hybrid material.

3.1.2. XRD and SEM Measurements

To analyze the evolution of the crystallinity and the morphology with the hybridization process we recorded the X-Ray diffractograms and the SEM images of the different materials. XRD diffractograms are plotted in Figure 2a,b and SEM images are in Figure 2c–f, respectively.

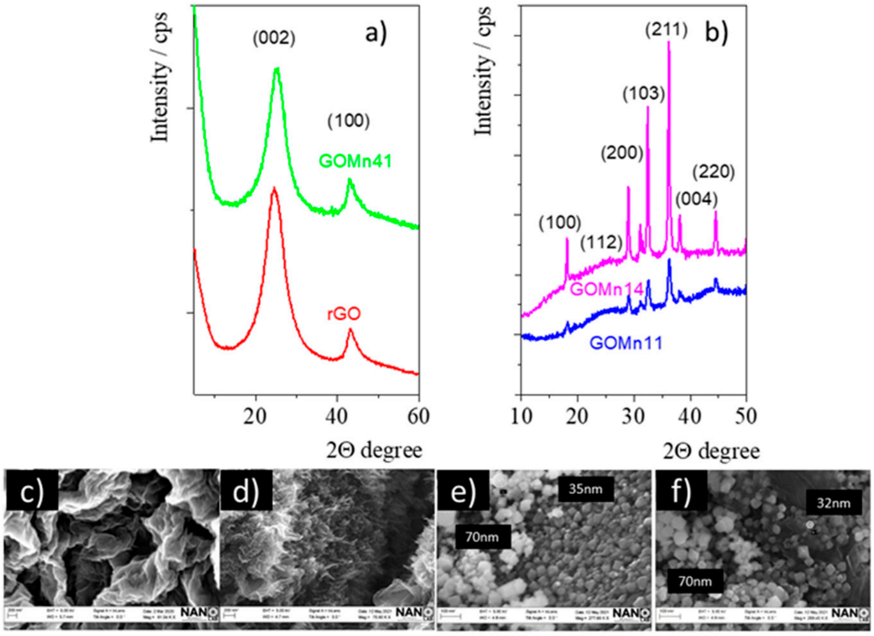

Figure 2. XRD diffractograms of (a) rGO and GOMn41 and (b) GOMn11 and GOMn14. SEM images of: (c) rGO (d) GOMn41 (e) GOMn11 and (f) GOMn14.

It is interesting to note that the diffractogram of the hybrid with the highest percentage of rGO (GOMn41), Figure 2a, is dominated by two broad peaks centered at 24.69° and 43.48° that can be attributed to diffractions corresponding to the (002) and (100) of graphene oxide (rGO) [57], however, the diffraction peaks corresponding to manganese oxide are not observed.

On the contrary, the diffractograms corresponding to the hybrids with a high proportion of Mn, GOMn11 and GOMn14 included in Figure 2b, are constituted by narrow peaks centered at 19.05°, 29.50°, 31.16°, 32.60°, 36.10° and 44.55° that can be assigned to the diffraction of the planes (101), (112), (103), (200), (211) and (220) in Mn_3O_4 [56].

To obtain information of the morphology of these hybrids, the SEM images of solid were taken, Figure 2c–f. As can be seen in Figure 2c,d, the samples with a high content of rGO show disordered and wrinkled platelets. These results are compatible with the diffractograms shown in Figure 2a, mainly dominated by the peaks corresponding to rGO. In the hybrids with high percentage of Mn_3O_4, Figure 2e,f corresponding to GOMn11 and GOMn14, respectively, show the presence of nanoparticles whose diameter are between 35 and 70 nm. This size is consistent with the Mn_3O_4 nanoparticles, obtained by other authors [43,63]. In this matrix of nanoparticles, dispersed graphene sheets can be observed forming a non-crystalline phase that would explain the background band observed in the diffractograms of Figure 2b.

3.2. Electrochemical Performances

3.2.1. Cyclic Voltammetry

Cyclic voltammetry (CV) was employed to evaluate the electrochemical properties of the electrodes prepared with the hybrid materials using a three-electrode system. Figure 3 illustrates the CV profiles obtained for rGO, GOMn41, GOMn11 and GOMn14 at two scan rates of 5 and 50 mV s^{-1} within the potential range of -1.5 to 0.2 V. The CV curve for rGO at 5 mVs^{-1} (Figure 3a) exhibits a pseudo-rectangular shape without any distinct Faradaic peak in this potential window. Typically, a rectangular CV shape is characteristic of carbonaceous materials which store charge through the formation of the electric double layer at the electrode-electrolyte interface [64]. However, a rounded shape is detected in the cycle, so some pseudocapacitive contribution due to the oxygenated functional can be intuited on rGO [64]. On the other hand, the CV curves for GO/Mn_3O_4 hybrids deviate from the rectangular shape, exhibit slight hump peaks at low potentials signature of pseudocapacitive behavior of the electrode materials.

Accordingly, it is possible to conclude that these hybrid materials exhibit both, pseudocapacitive behavior and electric double layer capacitor (EDLC) behavior. At 50 mV s^{-1}, Figure 3b, the peaks observed at low scan rate assigned to Faradaic reactions disappear, except for GOMn14 with the highest Mn content, in whose curve the deviation from the rectangular shape is slightly appreciated. At low scan rate (5 mVs^{-1}), there is ample time for redox reactions while at high scan rate, the diffusion of reagents through the pores of the material hinders the occurrence of redox reactions. Finally, when the Mn_3O_4 percentage increases, the CVs cycles become more symmetric indicating improved electrochemical behavior and charge store capabilities of the hybrid materials.

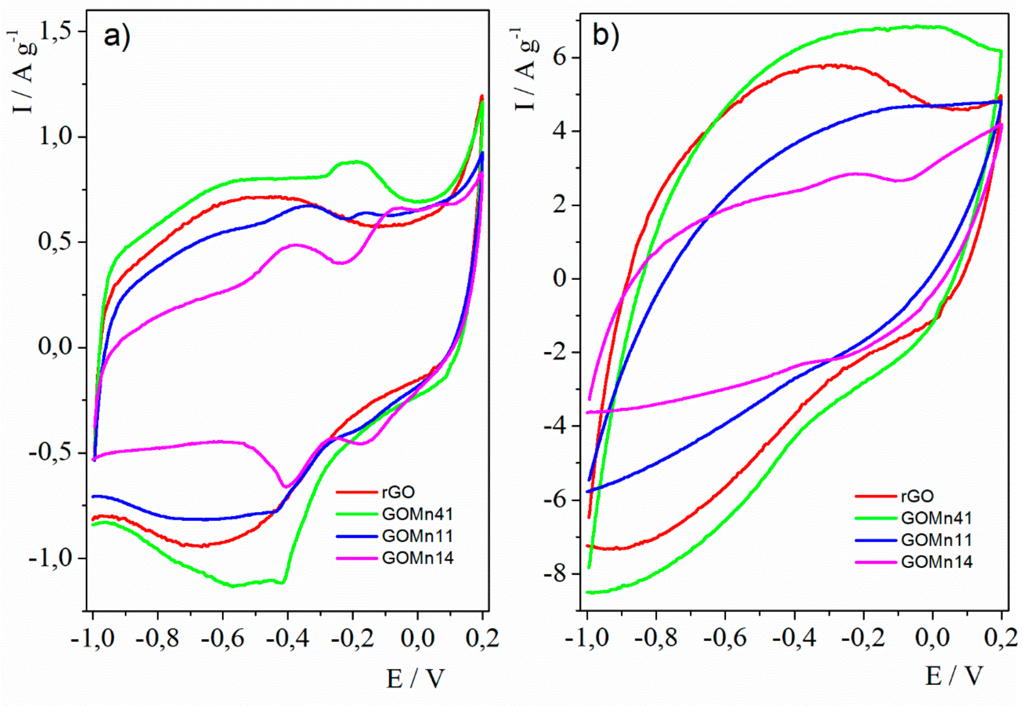

Figure 3. CV profiles at a) 5 mV s^{-1} and b) 50 mV s^{-1} for GO and GO/Mn_3O_4 hybrids.

3.2.2.. Galvanostatic Charge Discharge GCD

The energy density, power density, and specific capacitance of the hybrid materials were evaluated using the Galvanostatic Charge-Discharge (GCD) technique. Figure 4a displays the GCD curves obtained for rGO, GOMn41, GOMn11 and GOMn14 at a current density of 1 A g^{-1} performed between -1 and 0.2 V (vs Ag/AgCl) in 1M KOH solution. The GCD curves are not perfectly linear, which may be related to the coexistence of two mechanisms, the electric double layer and a pseudocapacitive mechanisms. As can be seen in Figure 4a, the charge-discharge time is clearly longer for GOMn41 hybrid than for rGO, and shorter in the case of the GOMn14 hybrid.

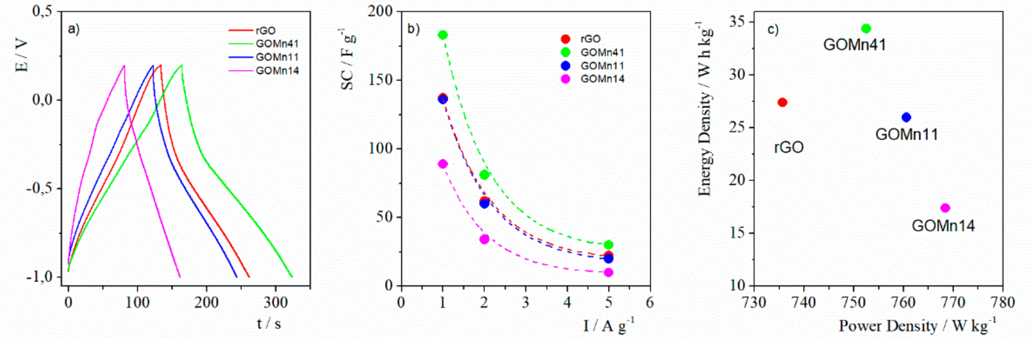

doi:10.20944/preprints202407.1586.v1

Figure 4. a) GCD curves for rGO and GO/Mn_3O_4 hybrids at 1A g^{-1}. b) Specific capacitance at varying current densities of 1, 2 and 5 A g^{-1}. The dashed lines are just visual guide. c) Ragone plot of rGO and GO/Mn_3O_4 hybrids.

The specific capacitances, SC, energy densities, E and power densities, P of the materials were calculated from GCD curves using the equations 1-3, respectively.

$$SC\ (F\ g^{-1}) = \frac{I\ \ \Delta t}{\Delta V\ \ m} \tag{1}$$

$$E\ (W\ h\ kg^{-1}) = \frac{1}{2}\frac{SC\ (\Delta V)^2}{3.6} \tag{2}$$

$$P\ (W\ kg^{-1}) = \frac{3600\ E}{\Delta t} \tag{3}$$

were SC representing the specific capacitance (F g^{-1}), I (A) is current, ΔV (V) is the total potential of the voltage window, Δt (s) is discharging time, and m (g) is the mas of the active electrode material.

The specific capacitance, energy and power densities values calculated from data obtained at a current density of 1 A g^{-1} are collected in Table 2. The SC values calculated were 137, 173, 136 and 89 F g^{-1} for rGO, GOMn41, GOMn11 and GOMn14 respectively.

The SC values obtained at different current density values are plotted in Figure 4b. They decreased by increasing the current density from 1 to 5 A g^{-1}. This can be due to the limited interaction time between electrolyte ions and the inner regions of the electrode material at elevated current densities [65], the ions have not opportunity to diffuse into the pores of the material [66].

The values obtained for energy and power densities have been collected in Table 2 and plotted in Figure 4c. The Ragone plot of rGO and GOMn_3O_4 hybrids (Figure 4c) provides the relationship between the energy and power densities. The SC retention after 500 charge-discharge cycles at 1 A $g^{-1}$are also in Table 2 and show that rGO/Mn_3O_4 composites have good cycle life as electrode material for supercapacitor since they maintain at least 71% of the initial SC.

Table 2. Specific capacitance in KOH 1M (SC), SC after 500 cycles and Energy and Power densities. Specific capacitance in Et4NBF4/CAN (2 electrodes cell). SC after 500 cycles, Energy and Power densities.

		KOH 1M (3 electrodes cell)			Et_4NBF_4/CAN (2 electrodes cell)
Materials	**SC (F g^{-1})**	**E (W h kg^{-1})**	**P (W kg^{-1})**	**SC retention after 500 cycles (%)**	**SC_{EDLC} (F g^{-1})**
rGO	137 ± 27	27	736	73 ± 15	90 ± 18
GOMn41	173 ± 34	34	753	76 ± 15	66 ± 13
GOMn11	136 ± 26	26	761	74 ± 15	35 ± 7
GOMn14	89 ± 17	17	768	71 ± 14	17 ± 3

4. Discussion

We are interested in analyzing the correlation between the specific capacitance (SC) in KOH 1M and the structural and textural properties. With this purpose in Figure 5a, the specific capacitance in a 3-electrodes cell, SC, is plotted against the specific surface area (SBET). To evaluate the contribution of the double-layer mechanism to the total specific capacitance, all materials were also tested in a 2-electrode cell with a symmetrical configuration using Et_4NBF_4/CAN as a non-aqueous electrolyte (Table 2). We have designated the values of SC thus obtained as SC_{EDLC} since pseudocapacitive reactions do not occur in an organic medium. Figure 5b shows the variation of the specific capacitance in 2-electrodes cell, SC_{EDLC}, with the O/C ratio calculated from XPS. Finally, as we expected Mn to be responsible for the Faradaic reactions, SC_{FR} estimated from $SC_{FR} = SC - SC_{EDLC}$ was plotted against the atomic percentage of Mn obtained from XPS measurements in Figure 5c.

As can be seen, the figures reveal interesting insights. Thus, Figure 5a shows a linear correlation between the specific capacitance and specific surface. This behavior agrees very well with results found for carbon-based supercapacitors [67,68]. Accordingly, GOMn41 with the highest S_{BET} shows the best performance as a supercapacitor electrode, while both, rGO and GOMn11, which share similar S_{BET} values, exhibit comparable specific capacitance values, ~ 136 F g^{-1}. A similar trend is observed when correlating specific capacitance with the micropore volume determined through CO_2 adsorption, see Table 1. This behavior was previously reported for carbonaceous materials [68] and was assigned to the existence of an electric double layer mechanism. The Authors considered that the inclusion of carbonaceous materials enhances specific surface area of the electrodes, facilitating the ion contact and promoting the EDLC mechanism, which relies on ion adsorption [68].

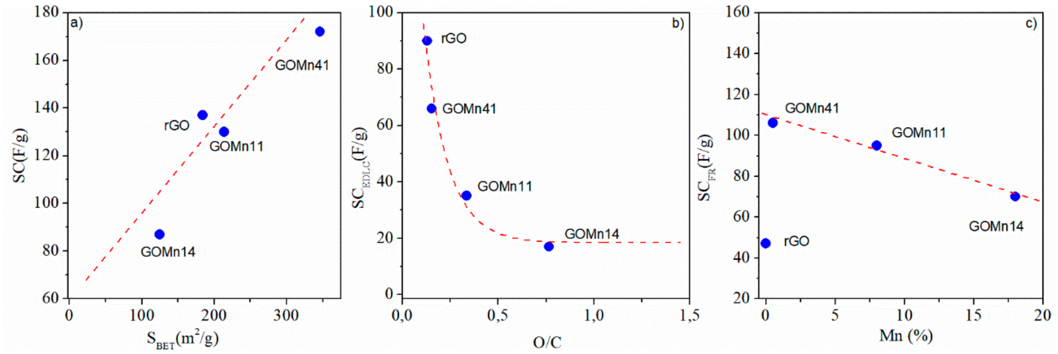

Figure 5. a) Specific capacitance in a 3-electrodes cell with KOH (SC) against the BET surface area (S_{BET}). b) Specific capacitance in 2-electrodes cell with Et_4NBF_4/CAN (SC_{EDLC}) against O/C. c) Subtraction $SC-SC_{EDLC} = SC_{FR}$ against percentage of atomic manganese. The dashed lines are just visual guides.

Figure 5b represents the specific capacitance values obtained in a two-electrode cell with Et_4NBF_4/CAN medium, SC_{EDLC}, against the O/C atomic ratio obtained by XPS (Table 1). As can be seen in Figure 5b, SC_{EDLC} shows a continuous decrease as the O/C ratio increases. Accordingly, rGO, which has the lowest O/C ratio, demonstrates the best electrochemical performance in this medium.

Although it is acknowledged that isolating the contribution of the electric double layer mechanism from that of Faradaic reactions to the total specific capacitance is challenging, we have attempted a naive approach to separate both contributions by calculating the difference between the SC values obtained in KOH medium using a three-electrode cell (SC) and those obtained in the organic medium using a two-electrode cell (SC_{EDLC}). This is an attempt to distinguish the Faradaic mechanism and explore its relationship with certain structural properties. Although Faradaic reactions can be expected to be favored by Mn content, Figure 5c shows that the SC_{FR} of the hybrids is always greater than the specific capacitance of rGO, however, the SC_{FR} decreases when the percentage of Mn increases.

As mentioned above, the hybrid with the lowest percentage of Mn, GOMn41, manages to improve the specific capacitance of rGO from 137 to 173 F g^{-1}, increases its energy density from 27 to 34 W h kg^{-1} and the power from 736 to 753 W kg^{-1}. Likewise, GOMn41 has the highest capacitance retention after 500 cycles at 1 A g^{-1}. As mentioned, this effect may be due on the one hand to the higher proportion of carbon which favors the EDLC effect, and on the other hand to the increase in the accessible surface of the material, thanks to the presence of Mn_3O_4 nanoparticles that serve as spacers, avoiding stacking of rGO sheets [69].

At hybrids with higher proportion of Mn_3O_4 nanoparticles, the specific capacitances decrease from 137 F g^{-1} of rGO to 136 and 89 F g^{-1} for GOMn11 and GOMn14 respectively, and the energy densities also decrease. The increase in Mn_3O_4 nanoparticles on the surface decreases the specific surface area (S_{BET}) due to the blocking of the pores, as observed in Table 1 and in the SEM images.

We can conclude that the presence of Mn nanoparticles favors the presence of Faradaic reactions and will increase the specific capacitance, to the extent that the specific surface area is not compromised.

5. Conclusions

In summary, we have synthesized supercapacitor electrode materials using $Mn(CH_3COO)_2$ and simultaneously reduced graphene oxide (rGO) through a sin-gle-step hydrothermal process.

The GOMn41 hybrid, characterized by the lowest percentage of Mn, demonstrates significantly enhanced capacitive performance compared to graphene oxide treated with hydrothermal methods, rGO, and present the highest capacitance retention after 500 cycles. This improvement is attributed to the unique structure achieved by com-bining rGO and Mn3O4 nanoparticles in a 4:1 weight ratio, resulting in a high specific surface area that enhances the initial specific capacitance of rGO. Hybrids with a higher proportion of Mn3O4 result in a less accessible structure probably due to pore blocking. The content of Mn3O4 nanoparticles favors the presence of Faradaic reactions and will increase the specific capacitance, if the specific surface area is not compro-mised. The results will shed light on the preparation of hybrid materials derived from Mn3O4 and reduced graphene oxide for using as supercapacitor electrodes.

Author Contributions: Conceptualization, DLD, MDM and MMV.; methodology, DLD, MDM and MMV; investigation, AG, DLD, MDM, MJSM, SDB and VFJ; data curation, DLD, MDM and MMV; writing original draft preparation, DLD, MDM, and MMV; writing review and editing, DLD, MDM, MMV and S. funding acquisition, MMV. All authors have read and agreed to the published version of the manuscript.

Funding: This research was funded by Junta de Castilla y León grant number SA106P23.

Acknowledgments: Vito Clèrico from NANOLAB, University of Salamanca for the SEM images. X-ray photoelectron spectroscopy service de la Universidad de Malaga for XPS facility and the X-Ray Diffraction service of the University of Salamanca for the XRD measurements.

Conflicts of Interest: The authors declare no conflict of interest.

Abbreviations

CAN: Acetonitrile
CV: Cyclic voltammetry
E: Energy density
EDLC: Electrochemical double layer capacitor
Et4NBF4: Tetraethylammonium tetrafluoroborate
G: Graphene
GCD: Galvanostatic charge-discharge measurements.
GO: Graphene oxide
rGO: Reduced graphene oxide
GOMn41: Hybrid with a 4/1 GO/ Mn(CH3COO)2 weight ratio.
GOMn11: Hybrid with a 1/1 GO/ Mn(CH3COO)2 weight ratio.
GOMn14: Hybrid with a 1/4 GO/ Mn(CH3COO)2 weight ratio.
P: Power density
SC: Specific capacitance obtained at 3-electrode cell in KOH
SCEDLC: Specific capacitance obtained at 2-electrode cell in organic medium.
SCFR: SC- SCEDLC
SEM: Scanning electron microscopy.
TMO: Transition Metal oxide
XPS: X-ray photoelectron spectroscopy
XRD: X-ray Powder Diffraction

References

1. Smol, J.P., Climate Change: A planet in flux. Nature, 2012. 483(7387): p. S12-S15.
2. Samuel, E., et al., Supersonically Sprayed Zn2SnO4/SnO2/CNT Nanocomposites for High-Performance Supercapacitor Electrodes. ACS Sustainable Chemistry & Engineering, 2019. 7(16): p. 14031-14040.
3. Lichchhavi, A. Kanwade, and P.M. Shirage, A review on synergy of transition metal oxide nanostructured materials: Effective and coherent choice for supercapacitor electrodes. Journal of Energy Storage, 2022. 55: p. 105692.
4. Şahin, M.E., F. Blaabjerg, and A. Sangwongwanich, A Comprehensive Review on Supercapacitor Applications and Developments. 2022. 15(3): p. 674.
5. Jing, W., et al., Battery-supercapacitor hybrid energy storage system in standalone DC microgrids: areview. IET Renewable Power Generation, 2017. 11(4): p. 461-469.
6. Sharma, A., et al., Mesoporous nickel cobalt hydroxide/oxide as an excellent room temperature ammonia sensor. Scripta Materialia, 2017. 128: p. 65-68.
7. Zhang, L.L. and X.S. Zhao, Carbon-based materials as supercapacitor electrodes. Chemical Society Reviews, 2009. 38(9): p. 2520-2531.
8. Balducci, A., et al., High temperature carbon–carbon supercapacitor using ionic liquid as electrolyte. Journal of Power Sources, 2007. 165(2): p. 922-927.
9. Ragone, D.V., Review of Battery Systems for Electrically Powered Vehicles. 1968, SAE International.
10. Afif, A., et al., Advanced materials and technologies for hybrid supercapacitors for energy storage – A review. Journal of Energy Storage, 2019. 25: p. 100852.
11. Kibona, T.E., et al., Specific capacitance–pore texture relationship of biogas slurry mesoporous carbon/MnO2 composite electrodes for supercapacitors. Nano-Structures & Nano-Objects, 2019. 17: p. 21-33.
12. Lebedeva, M.V., et al., Micro–mesoporous carbons from rice husk as active materials for supercapacitors. Materials for Renewable and Sustainable Energy, 2015. 4(4): p. 20.
13. Kibona Enock, T., C.K. King'ondu, and A. Pogrebnoi, Effect of biogas-slurry pyrolysis temperature on specific capacitance. Materials Today: Proceedings, 2018. 5(4, Part 2): p. 10611-10620.
14. Zhang, Y., et al., A carbon-based 3D current collector with surface protection for Li metal anode. Nano Research, 2017. 10(4): p. 1356-1365.
15. Gong, Y., et al., Influence of graphene microstructures on electrochemical performance for supercapacitors. Progress in Natural Science: Materials International, 2015. 25(5): p. 379-385.
16. Stoller, M.D., et al., Graphene-Based Ultracapacitors. Nano Letters, 2008. 8(10): p. 3498-3502.
17. Ghosh, S., et al., Supercapacitive vertical graphene nanosheets in aqueous electrolytes. Nano-Structures & Nano-Objects, 2017. 10: p. 42-50.
18. Ke, Q. and J. Wang, Graphene-based materials for supercapacitor electrodes – A review. Journal of Materiomics, 2016. 2(1): p. 37-54.
19. Bonaccorso, F., et al., Graphene, related two-dimensional crystals, and hybrid systems for energy conversion and storage. Science, 2015. 347(6217): p. 1246501.
20. Chodankar, N.R., S.-H. Ji, and D.-H. Kim, Surface Modified Carbon Cloth via Nitrogen Plasma for Supercapacitor Applications. Journal of The Electrochemical Society, 2018. 165(11): p. A2446.
21. Al-Asadi, A.S., et al., Aligned carbon nanotube/zinc oxide nanowire hybrids as high performance electrodes for supercapacitor applications. Journal of Applied Physics, 2017. 121(12).
22. Futaba, D.N., et al., Shape-engineerable and highly densely packed single-walled carbon nanotubes and their application as super-capacitor electrodes. Nature Materials, 2006. 5(12): p. 987-994.
23. Yang, Z., et al., Carbon nanotube- and graphene-based nanomaterials and applications in high-voltage supercapacitor: A review. Carbon, 2019. 141: p. 467-480.
24. Inamdar, A.I., et al., Chemically grown, porous, nickel oxide thin-film for electrochemical supercapacitors. Journal of Power Sources, 2011. 196(4): p. 2393-2397.
25. Liu, H., et al., Transition metal based battery-type electrodes in hybrid supercapacitors: A review. Energy Storage Materials, 2020. 28: p. 122-145.
26. Zhu, Y., et al., Strong synergetic electrochemistry between transition metals of α phase Ni−Co−Mn hydroxide contributed superior performance for hybrid supercapacitors. Journal of Power Sources, 2019. 412: p. 559-567.
27. Mohd Abdah, M.A.A., et al., Review of the use of transition-metal-oxide and conducting polymer-based fibres for high-performance supercapacitors. Materials & Design, 2020. 186: p. 108199.
28. Kötz, R. and M. Carlen, Principles and applications of electrochemical capacitors. Electrochimica Acta, 2000. 45(15): p. 2483-2498.
29. Zeng, Y., et al., Oxygen-Vacancy and Surface Modulation of Ultrathin Nickel Cobaltite Nanosheets as a High-Energy Cathode for Advanced Zn-Ion Batteries. Advanced Materials, 2018. 30(33).
30. Zhang, H., et al., Flexible rechargeable Ni//Zn battery based on self-supported NiCo2O4 nanosheets with high power density and good cycling stability. Green Energy & Environment, 2018. 3(1): p. 56-62.

31. Chodankar, N.R., et al., Direct growth of FeCo2O4 nanowire arrays on flexible stainless steel mesh for high-performance asymmetric supercapacitor. NPG Asia Materials, 2017. 9(8): p. e419-e419.
32. Jiang, D.B., et al., One-pot synthesis of η-Fe2O3 nanospheres/diatomite composites for electrochemical capacitor electrodes. Materials Letters, 2018. 215: p. 23-26.
33. Chodankar, N.R., et al., Superfast Electrodeposition of Newly Developed RuCo2O4 Nanobelts over Low-Cost Stainless Steel Mesh for High-Performance Aqueous Supercapacitor. Advanced Materials Interfaces, 2018. 5(15): p. 1800283.
34. Zhu, Y., et al., 3D interconnected ultrathin cobalt selenide nanosheets as cathode materials for hybrid supercapacitors. Electrochimica Acta, 2018. 269: p. 30-37.
35. Verma, S., V.K. Pandey, and B. Verma, Facile synthesis of graphene oxide-polyaniline-copper cobaltite (GO/PANI/CuCo2O4) hybrid nanocomposite for supercapacitor applications. Synthetic Metals, 2022. 286: p. 117036.
36. Choudhury, N.A., S. Sampath, and A.K. Shukla, Hydrogel-polymer electrolytes for electrochemical capacitors: an overview. Energy & Environmental Science, 2009. 2(1): p. 55-67.
37. Yang, H., et al., Influences of graphene oxide support on the electrochemical performances of graphene oxide-MnO2 nanocomposites. Nanoscale Research Letters, 2011. 6(1): p. 531.
38. Repp, S., et al., Synergetic effects of Fe3+ doped spinel Li4Ti5O12 nanoparticles on reduced graphene oxide for high surface electrode hybrid supercapacitors. Nanoscale, 2018. 10(4): p. 1877-1884.
39. Elmouwahidi, A., et al., Carbon-TiO2 composites as high-performance supercapacitor electrodes: Synergistic effect between carbon and metal oxide phases. Journal of Materials Chemistry A, 2018. 6(2): p. 633-644.
40. Arshad, F., et al., Microwave-mediated synthesis of tetragonal Mn3O4 nanostructure for supercapacitor application. Environmental Science and Pollution Research, 2023. 30(28): p. 71464-71471.
41. Yang, L.W. and I. Zhitomirsky, Influence of Capping Agents on the Synthesis of Mn3O4 Nanostructures for Supercapacitors. ACS Applied Nano Materials, 2023. 6(6): p. 4428-4436.
42. Chen, R. and I. Zhitomirsky, Colloidal methods for the fabrication of Mn3O4-graphene film and bulk supercapacitors. Materials Letters, 2023. 335: p. 133811.
43. Beknalkar, S.A., et al., Mn3O4 based materials for electrochemical supercapacitors: Basic principles, charge storage mechanism, progress, and perspectives. Journal of Materials Science & Technology, 2022. 130: p. 227-248.
44. Wu, Y., et al., A novel solvothermal synthesis of Mn3O4/graphene composites for supercapacitors. Electrochimica Acta, 2013. 90: p. 210-218.
45. Wang, B., et al., Mn3O4 nanoparticles embedded into graphene nanosheets: Preparation, characterization, and electrochemical properties for supercapacitors. Electrochimica Acta, 2010. 55(22): p. 6812-6817.
46. Fan, Y., et al., One-pot hydrothermal synthesis of Mn3O4/graphene nanocomposite for supercapacitors. Materials Letters, 2013. 95: p. 153-156.
47. Liu, Y., et al., Graphene and Nanostructured Mn3O4 Composites for Supercapacitors. Integrated Ferroelectrics, 2013. 144(1): p. 118-126.
48. Zhang, W., et al., High performance Flower-Like Mn3O4/rGO composite for supercapacitor applications. Journal of Electroanalytical Chemistry, 2022. 910: p. 116170.
49. Centeno, T.A. and F. Stoeckli, Surface-related capacitance of microporous carbons in aqueous and organic electrolytes. Electrochimica Acta, 2011. 56(21): p. 7334-7339.
50. Wang, T., et al., Preparation of Porous Graphene@Mn3O4 and Its Application in the Oxygen Reduction Reaction and Supercapacitor. ACS Sustainable Chemistry & Engineering, 2019. 7(1): p. 831-837.
51. Jia, H., et al., Designing oxygen bonding between reduced graphene oxide and multishelled Mn3O4 hollow spheres for enhanced performance of supercapacitors. Journal of Materials Chemistry A, 2019. 7(12): p. 6686-6694.
52. Hidalgo, R.S., D. López-Díaz, and M.M. Velázquez, Graphene Oxide Thin Films: Influence of Chemical Structure and Deposition Methodology. Langmuir, 2015. 31(9): p. 2697-2705.
53. Claramunt, S., et al., The Importance of Interbands on the Interpretation of the Raman Spectrum of Graphene Oxide. The Journal of Physical Chemistry C, 2015. 119(18): p. 10123-10129.
54. López-Díaz, D., et al., Evolution of the Raman Spectrum with the Chemical Composition of Graphene Oxide. The Journal of Physical Chemistry C, 2017. 121(37): p. 20489-20497.
55. López-Diaz, D., M.D. Merchán, and M.M. Velázquez, The behavior of graphene oxide trapped at the air water interface. Advances in Colloid and Interface Science, 2020. 286: p. 102312.
56. Zhou, D., et al., Graphene-manganese oxide hybrid porous material and its application in carbon dioxide adsorption. Chinese Science Bulletin, 2012. 57(23): p. 3059-3064.
57. Huang, H.-H., et al., Structural Evolution of Hydrothermally Derived Reduced Graphene Oxide. Scientific Reports, 2018. 8(1): p. 6849.
58. Dubinin, M.M., Adsorption properties and microporous structures of carbonaceous adsorbents. Carbon, 1987. 25(5): p. 593-598.

59. Nguyen, C. and D.D. Do, The Dubinin–Radushkevich equation and the underlying microscopic adsorption description. Carbon, 2001. 39(9): p. 1327-1336.
60. Lee, S.W., et al., Carbon Nanotube/Manganese Oxide Ultrathin Film Electrodes for Electrochemical Capacitors. ACS Nano, 2010. 4(7): p. 3889-3896.
61. López-Díaz, D., et al., Towards Understanding the Raman Spectrum of Graphene Oxide: The Effect of the Chemical Composition. Coatings, 2020. 10(6).
62. Radinger, H., et al., Manganese Oxide as an Inorganic Catalyst for the Oxygen Evolution Reaction Studied by X-Ray Photoelectron and Operando Raman Spectroscopy. ChemCatChem, 2021. 13(4): p. 1175-1185.
63. Noviyanto, A., et al., Anomalous Temperature-Induced Particle Size Reduction in Manganese Oxide Nanoparticles. ACS Omega, 2023. 8(47): p. 45152-45162.
64. Oh, Y.J., et al., Oxygen functional groups and electrochemical capacitive behavior of incompletely reduced graphene oxides as a thin-film electrode of supercapacitor. Electrochimica Acta, 2014. 116: p. 118-128.
65. Ren, G., et al., Carbon nanotube@Mn3O4 composite as cathode for high-performance aqueous zinc ion battery. Journal of Alloys and Compounds, 2022. 898: p. 162747.
66. Mohammadi, S. and S.M. Mousavi-Khoshdel, Preparation of a Cu-Doped Graphene Oxide–Glutamine Nanocomposite for Supercapacitor Electrode Applications: An Experimental and Theoretical Study. ACS Applied Electronic Materials, 2024. 6(6): p. 4108-4119.
67. Lobato, B., et al., Capacitance and surface of carbons in supercapacitors. Carbon, 2017. 122: p. 434-445.
68. Kwak, C.H., D. Kim, and B.C. Bai Correlation of EDLC Capacitance with Physical Properties of Polyethylene Terephthalate Added Pitch-Based Activated Carbon. Molecules, 2022. 27. https://doi.org/10.3390/molecules27041454.
69. Khan, M.S., et al., Unveiling the electrochemical advantages of a scalable and novel aniline-derived polybenzoxazole-reduced graphene oxide composite decorated with manganese oxide nanoparticles for supercapacitor applications. Journal of Energy Storage, 2023. 73: p. 109109.